Supporting Information for Proximity Induced High Temperature Magnetic Order in Topological Insulator - Ferrimagnetic Insulator Heterostructure

Murong Lang,[†,ll,] Mohammad Montazeri,[†,ll] Mehmet C. Onbasli,[‡] Xufeng Kou,[†] Yabin Fan,[†] Pramey Upadhyaya,[†] Kaiyuan Yao,[†] Frank Liu,[‡] Ying Jiang,[#] Wanjun Jiang,[†] Kin L. Wong,[†] Guoqiang Yu,[†] Jianshi Tang,[†] Tianxiao Nie,[†] Liang He,[†,*] Robert N. Schwartz,[†] Yong Wang,[#] Caroline A. Ross,[‡] and Kang L. Wang[†,*]*

[†] Department of Electrical Engineering, University of California, Los Angeles, California 90095, USA

[‡] Department of Materials Science and Engineering, Massachusetts Institute of Technology, Cambridge, Massachusetts 02139, USA

[#] Center of Electron Microscopy, State Key Laboratory of Silicon Materials, Department of Materials Science and Engineering, Zhejiang University, Hangzhou, 310027, China

[ll] These authors contribute equally to this work.

* To whom correspondence should be addressed.

E-mail: *langmr@ucla.edu,wang@seas.ucla.edu,liang.heliang@gmail.com*

Supporting Information

S1. Sample growth and TEM characterization methods

i. YIG/GGG Substrate Growth and Characterization.

Before pulsed laser deposition of YIG films, stoichiometric YIG targets were prepared by mixing Y_2O_3 and iron oxide, ball milling, calcination and sintering at 1400 ℃. 50 nm-thick YIG films were pulsed-laser deposited on 10mm x 10 mm Gallium Gadolinium Garnet (GGG) (111) substrates (Supplier: MTI Crystals Inc.) under 5 mTorr oxygen pressure (3 μTorr base pressure) using a KrF Coherent excimer laser with 400 mJ pulses at 2 Hz pulse rate at 650°C with 18,000 laser shots. After growth, the chamber was cooled in oxygen ambient. Low deposition rate (< 1nm/min) and similar lattice parameters of YIG and GGG (mismatch < 0.2%) allow epitaxial and low surface-roughness (< 0.3 nm rms) growth of YIG films on substrates. The Nanoscope IV atomic force microscope was used to probe surface roughness, quality and phases by driving a silicon cantilever in tapping mode operation at 2 Hz scan rate. Phase and amplitude information of the tip movement was recorded. A PANalytical Xpert X-ray diffractometer was used to measure x-ray scattering of films in ω-2θ scans between 2θ =40° to 130°. XRD analysis was done by using HighScore Plus X-ray analysis software.

ii. Growth of Bi_2Se_3 Thin Films.

High-quality single crystalline Bi_2Se_3 thin films growth were conducted in a PerkinElmer MBE system. High-purity Bi (99.9999%) was evaporated from conventional effusion cells at 470 ℃, while Se (99.99%)was formed from a cracker cell from SVTA at 240℃, and the YIG/GGG (111) substrate was kept at 200℃ during the growth. The pseudomorphic growth of Bi_2Se_3 was monitored by real-time reflection high energy

electron diffraction (RHEED). A 2 nm Al was *in-situ* evaporated to immediately after the growth of TI film in MBE chamber to protect the film for oxidation and environmental doping.[1, 2]

iii. TEM Characterization.

The cross-sectional TEM foils of Bi_2Se_3/YIG/GGG were prepared by focused ion beam (FIB, Quanta 3D FEG, FEI). Pt capping layer was deposited on Bi_2Se_3 film to protect it from ion damage during the milling by FIB. All parameters were carefully optimized to avoid the ion injection and specimen damage, including the accelerating voltage, beam current and tilt angle. The interface and crystalline structure were characterized by high-resolution STEM experiments, carried out on a FEI Cs corrected Titan operating at 200 kV. The high angle annular dark field (HAADF) images were acquired by a Fischione HAADF detector.

S2. EDX mapping of Bi_2Se_3/YIG/GGG heterostructure

The Bi_2Se_3/YIG/GGG interface and crystalline structure were characterized by high-resolution STEM and EDX mapping experiments, carried out on a FEI Probe Cs corrected Titan operating at 200 kV. The high angle annular dark field (HAADF) images were acquired by a Fischione HAADF detector and the EDX maps were acquired by ChemiSTEM Technology with four windowless SDD detectors. The typical STEM-HAADF image of Bi_2Se_3/YIG grown on GGG is shown in **Fig. S1a**. Specifically, the colored distribution maps of each individual element are shown in **Figs. S1b-h**. All the elements display a distinct distribution pattern: Bi, Se locate at the top of the map; Y and Fe

locates at the middle; Gd and Ga locate at the bottom; O locates at the middle and bottom part of the map. The distribution of every element is uniform and there is no inter diffusion between two layers.

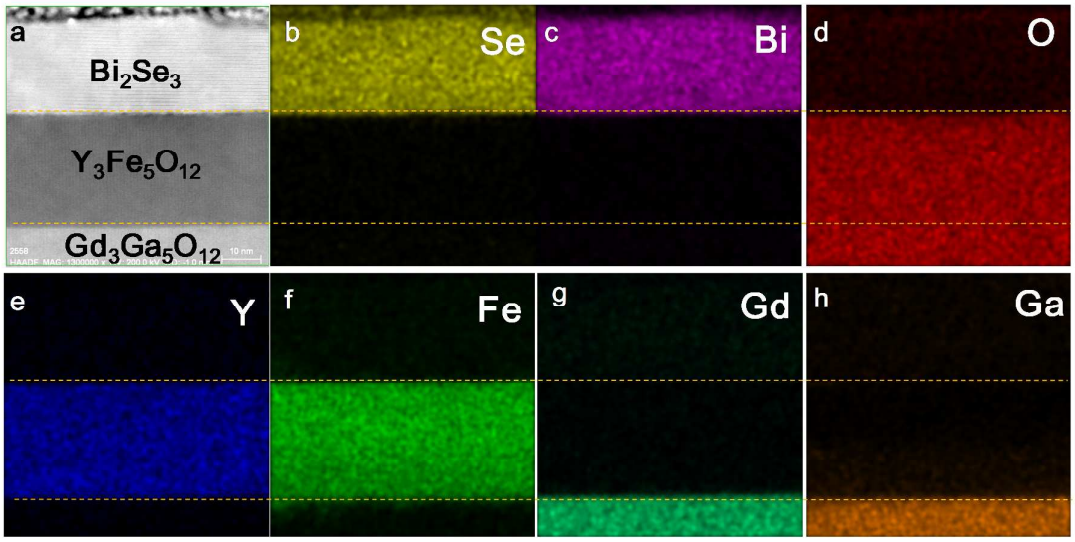

Figure S1.**a**, STEM-HAADF image of Bi_2Se_3/YIG grown on GGG. **b-h**, EDX maps of individual element Bi **(b)**, Se **(c)**, O **(d)**, Y **(e)**, Fe **(f)**, Gd **(g)** and Ga **(h)**, corresponding to the area of **(a)**.

Quantitative maps (QMaps) showing the atomic concentration of elements based on the quantification result of each pixel, indicating there is no intermixing at the interface as shown in **Fig. S2**. Multiple linescans have been acquired to verify the interface.

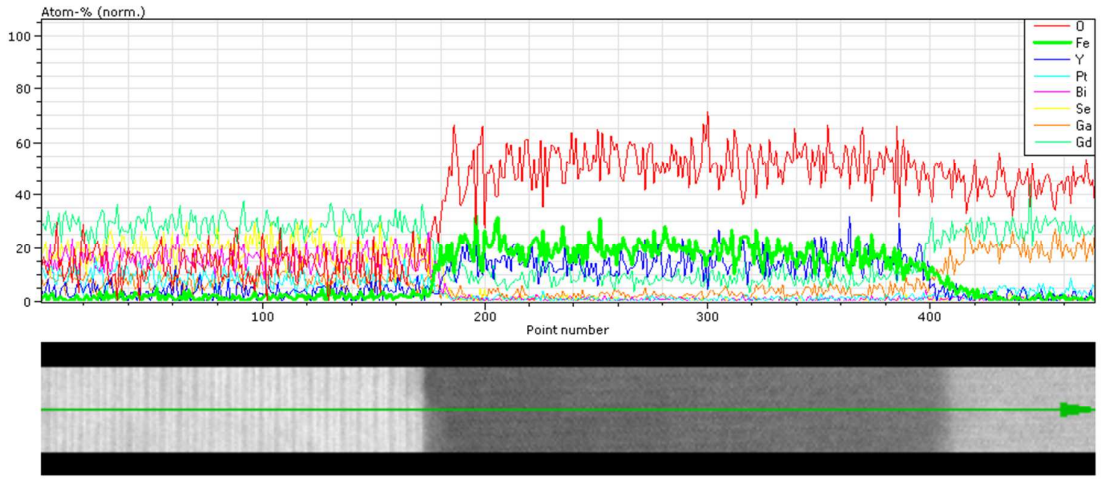

Figure S2. Atomic concentration of elements based on the quantification result of each pixel, indicating there is no intermixing at the interface.

S3. Device fabrication and electrical characterization methods.

The Bi_2Se_3/YIG/GGG thin films were patterned into a micrometer-scale Hall bar geometry using conventional optical photolithography and a subsequent CHF_3 dry etching of 20 s. Six Hall channel contacts (10 nm titanium and 100 nm gold) were defined by e-beam evaporation. Standard four-terminal electrodes were fabricated to eliminate the contact resistance. A constant AC current of 0.05 ~ 0.1 μA with a frequency of 1300 Hz is fed through two outer contacts, and the voltage drop across inner pads is measured to determine the resistance. The transport measurements were carried out with PPMS with rotatable magnetic field. The temperature range is from 1.9 K ~ 300 K and the magnetic field can be up to ±90 kOe.

S4. Temperature dependence of longitudinal resistance and carrier density

Fig. S3a provides temperature dependence of longitudinal resistance in linear and logarithmic (inset) scales. The channel resistance initially decreases with the temperature, showing a typical metallic behavior in the temperature range of 50~300 K,[3-5] in which the phonon scattering dominates (**Fig. S3a**). When the temperature drops below 50 K, the resistance experiences an increase, primarily due to the carrier freeze-out effect similar to those observed in lightly-doped Bi_2Se_3.[5] We have attempted to extract the activation energy E_a in the temperature range of 2~50 K, where a nearly linear relation exists for $R \sim e^{E_a/k_BT}$

(**Fig. S3a inset**, logarithmic scale). Here, R stands for the channel resistance, k_B is the Boltzmann constant and T is the measurement temperature. It is noted that our fitting result yields only a small activation energy less than 1 meV, which cannot be simply explained by the impurity levels in Bi_2Se_3. Instead, at this temperature range the surface conduction can be enhanced compared to that at higher temperatures, thus becoming a non-negligible component. Hall carrier densities n_H are extracted from $n_H = (R_H e)^{-1}$,where R_H is the Hall slope, e is the electron charge. In **Fig. S3b**, the carrier density reduces as temperature decreases in the temperature range of 2 ~ 100 K, resulting in the dominance of surface transport at low temperature.

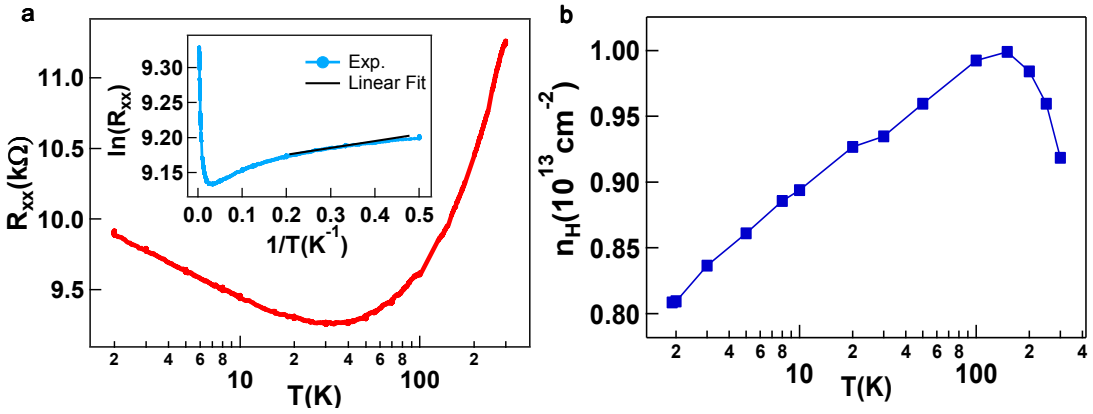

Figure S3. a, Temperature dependence of longitudinal resistance in linear and logarithmic (inset) scales. **b**, Hall carrier densities as a function of temperature, extracted from the Hall traces at ±4 T at each temperature point.

S5. Temperature dependence of MR ratio and H_s in magnetoresistance

In order to clearly investigate the temperature dependence of the hysteretic magnetoresistance (MR) in Bi_2Se_3/YIG, the detailed analysis is performed as shown in **Fig. S4**. The MR ratio used to characterize the hysteretic behavior in MR, is defined as

(R_{max}-R_s)/R_{max}×100%, where R_{max} and R_s are obtained from ΔMR after background subtraction. Here, R_{max} presents the maximum resistance in ΔMR, while R_s is the resistance at saturation region. For both out-of-plane and in-plane case, the MR ratio reduces as temperature increases as shown in the red curve in **Figs. S4a-b**, suggesting that the diminishing of the hysteretic signal at $T > 25$ K is presumably due to the dominant transport through the bulk Bi_2Se_3 channel. Moreover, the temperature dependences of H_s for both out-of-plane and in-plane field are consistent with the MOKE results. With out-of-plane magnetic field (**Fig. S4a** blue curve), H_s increases as temperature arises; while with in-plane magnetic field (**Fig. S4b**), H_s decreases as temperature increases.

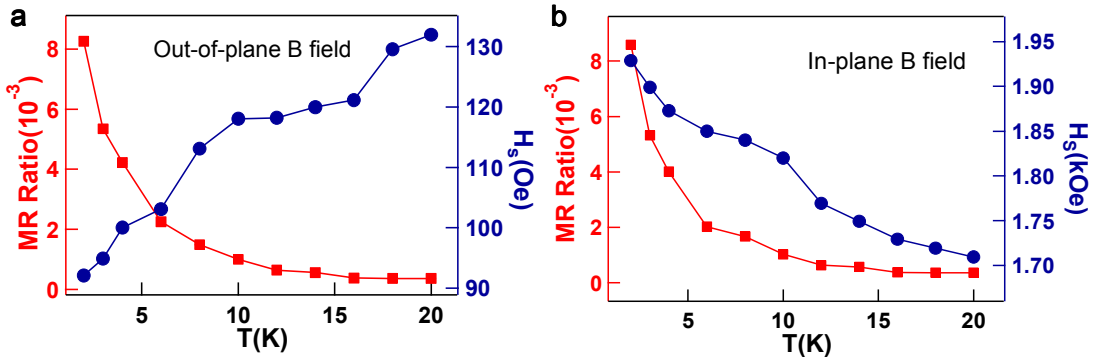

Figure S4. **a-b**, MR ratio and H_s as a function of temperature with out-of-plane (a) and in-plane magnetic field (b) applied.

S6. Magnteotransport data of other TI/YIG samples

We have measured magnetotransport of several different 8 QL TI/YIG samples with out-of-plane and in-plane field in PPMS, all of them showing consistent/similar hysteretic behaviors as shown in **Figs. S5** (sample #2) and **S6** (sample #3). The magnetoresistances of sample #2 with in-plane field along longitudinal and transverse direction are shown in **Figs.**

S5 a and **b,** respectively. We also measured DC current dependence of sample #3 with a perpendicular field and an in-plane applied, as shown in **Figs. S6 a** and **b**.

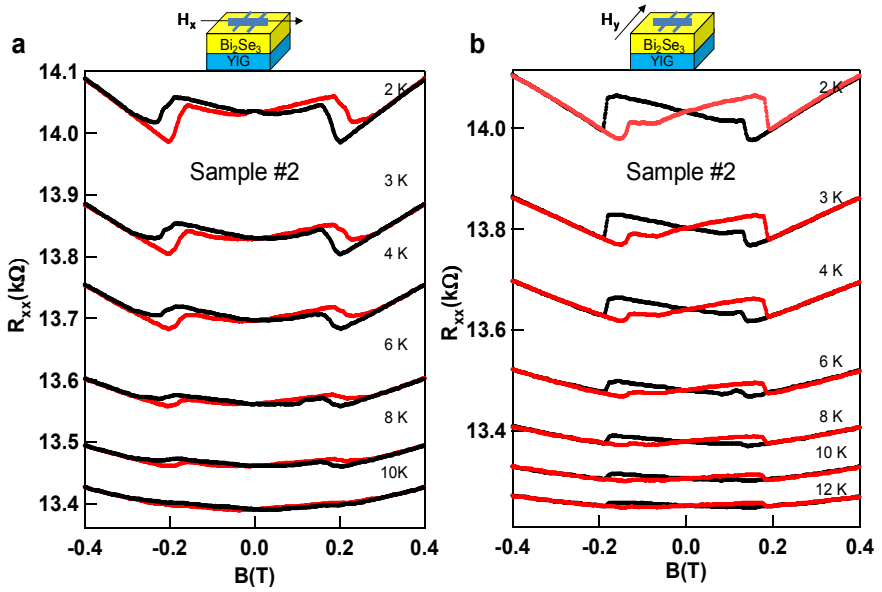

Figure S5. Magneto transport results of sample #2 with in-plane field along (**a**) longitudinal and (**b**) transverse direction applied

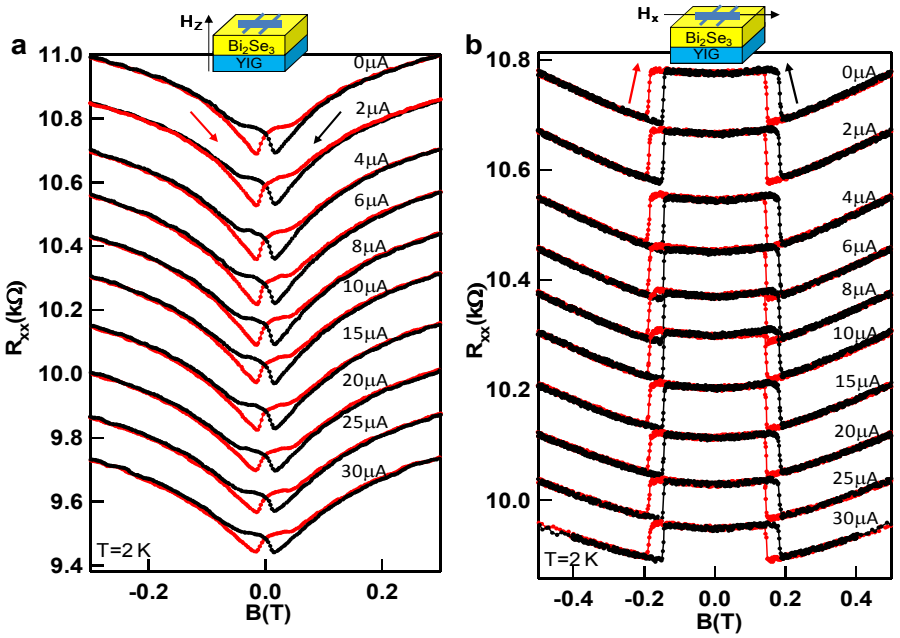

Figure S6. DC current dependence of magnetoresistance in sample #3 with (**a**) perpendicular and (**b**) transverse magnetic field applied.

S7. Polar and longitudinal MOKE measurement setup

Magneto-optical Kerr effect (MOKE) describes rotation of polarization plane of a reflected light with respect to the linearly polarized incident light due to its interaction with the magnetic moment of the reflector and thus can be used to directly probe the magnetization of materials; a well-established experimental technique. In our measurements, we used linear polarized 750 nm laser beam for incident light and employed a Wollaston prism along with Si balanced photodetector to resolve the Kerr rotation (see **Figs. S7a-b**). While the Kerr rotation with out-of-plane external field and normally incident light (Polar MOKE) is dominated by the out-of-plane component of the magnetic moment, the geometry of in-plane magnetic field and angled incident light (Longitudinal MOKE) can reveal field-dependent behavior of the in-plane component of the magnetic moment as well. The magnetic field range we applied is ± 6 kOe.

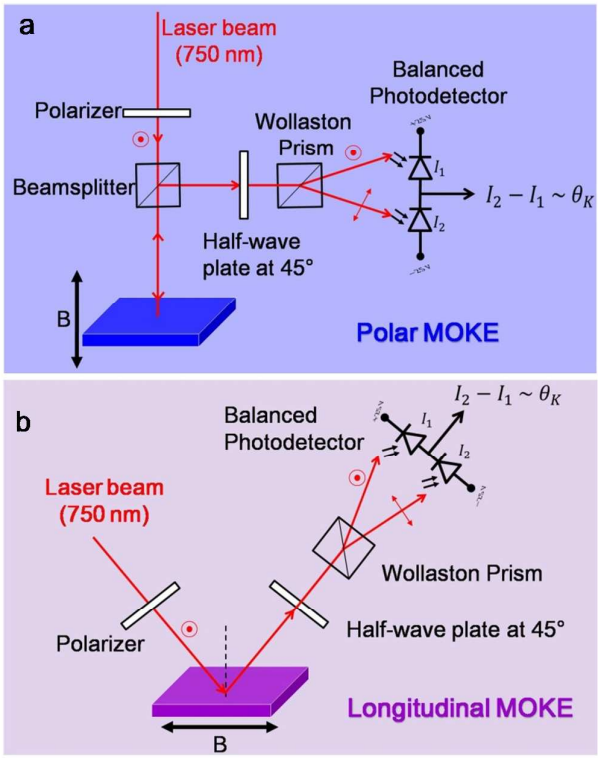

Figure S7. a-b, Polar **(a)** and longitudinal **(b)** MOKE measurement setup

S8.Comprehensive temperature dependence of Polar and Longitudinal MOKE of YIG

We show comprehensive temperature dependent polar and longitudinal MOKE of YIG in **Figs. S8a-b**. The magnetization of YIG substrate is tilted from perfect in-plane to canted out-of-plane during cooled down process. This can be confirmed by comparing the saturation field (H_s) of polar and longitudinal MOKE hysteresis loops. The H_s obtained from polar MOKE data **(Fig. S8a)** increases as temperature arises, as summarized in the red curve in **Fig. S8c**. While the H_s of longitudinal mode hysteresis loops **(Fig. S8b)** decreases as temperature increases, indicated by the blue curve **Fig. S8c**. The opposite temperature dependence of H_s for the polar and longitudinal modes is mainly due to the fact that the out-of-plane anisotropy is weakened while the in-plane anisotropy is enhanced as

temperature increases. It should be noted that for temperature >200 K, the out-of-plane moment cannot be measured by MOKE within the range of available magnetic field ~6 kOe.

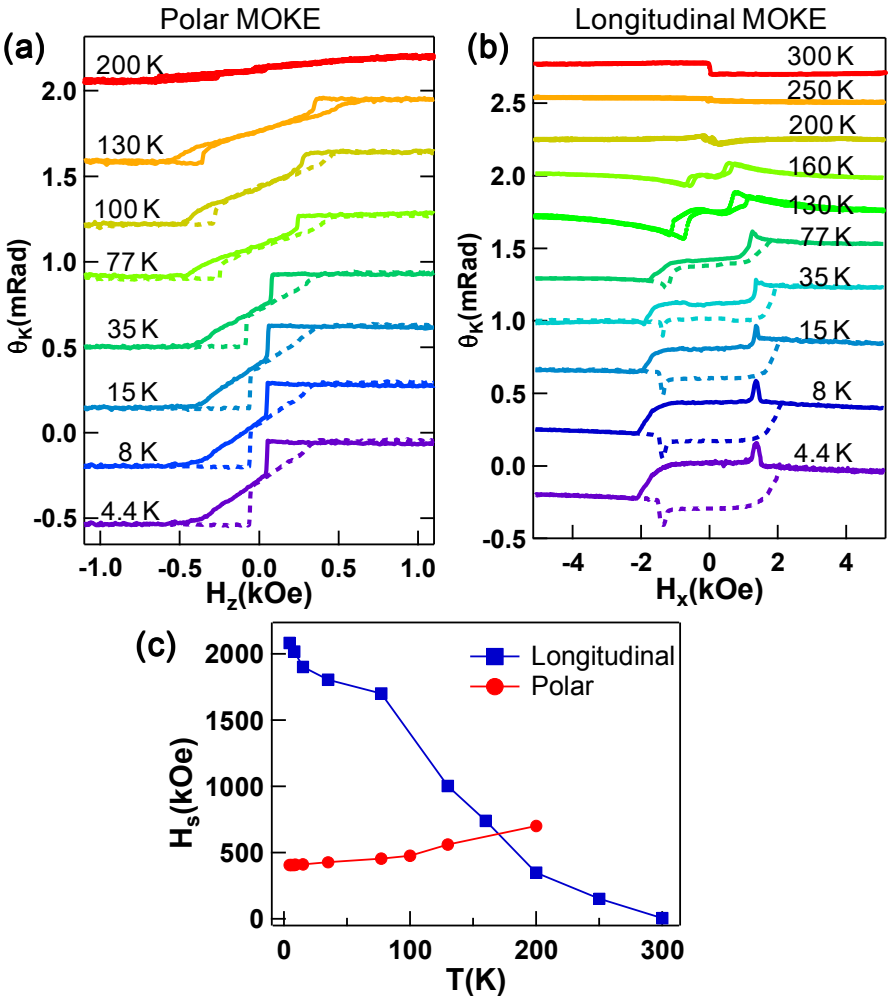

Figure S8. **a-b**, Temperature dependence of polar **(a)** and longitudinal **(b)** MOKE of YIG substrate. All curves are vertically shifted for clarification. **c**, Saturation field as a function of temperature, extracted from the hysteresis loops from **a-b**. Blue curve indicates the longitudinal mode, and the red curve indicates the polar mode.

S9. Magnetic anisotropy of YIG/GGG at low temperature

The YIG anisotropy includes three components: a shape anisotropy, favoring in plane magnetization; a magnetocrystalline anisotropy, favoring magnetization along the <111> axis which are at 90˚ and 35˚ to the film plane due to the negative K_1 at low temperature; and a magnetoelastic anisotropy which favors out-of-plane magnetization because the YIG is under in-plane tension due to thermal mismatch with GGG. Based on bulk values of saturation magnetization, magnetocrystalline anisotropy constants, magnetostriction[6], lattice parameters[7] and thermal expansion coefficients of the YIG and GGG[8, 9], the shape anisotropy is the dominant term (for M = 160 kA/m, K_{sh} = 1.6×10^4 J/m^3) promoting an in-plane easy axis at low temperatures. The magnetoelastic term is small because both the magnetostriction coefficient and the strain of the YIG are small. The YIG and GGG lattice parameters are well matched at room temperature, 12.376 Å for YIG, 12.375 Å for GGG[7], but GGG has a larger thermal expansion, $\alpha = 10.4\times10^{-6}$ for YIG, 8.96×10^{-6} for GGG at room temperature[8], so the YIG will be under in-plane tensile strain and out-of-plane compressive strain at low temperature. The magnetostriction λ_{111} = -2.5×10^{-6} at 4 K[6] and Young's modulus of 200 GPa[10] leads to a weak out of plane anisotropy. The magnetocrystalline anisotropy K_1 = -2500 J/m^3 at 4 K[6] is expected to produce a small canting of the magnetization along the out-of-plane direction.

A micromagnetic model of a 50 nm thick, 1 μm square of YIG using parameters characteristic of YIG at low temperature is shown in **Fig. S9** for an out-of-plane field. The model used the OOMMF code from NIST with cell sizes of 5 nm by 5 nm (in plane) by 25 nm (in the out-of-plane direction). M_s was 175 kA/m, K_1 was -2500 J/m^3, and damping constant was 0.5. The model included magnetocrystalline anisotropy, which required a

coordinate rotation of the film to model the (111) orientation of the film, but magnetoelastic anisotropy was neglected. The model showed little remanence, but did reproduce hysteretic features near saturation similar to those seen in the polar MOKE data of YIG/GGG, and which were associated with the magnetization direction changing from the <111> out of plane direction to a <111> direction closer to the film plane as the field decreased.

The calculations predict a predominantly in plane magnetization at remanence with a small out of plane canting resulting from the magnetocrystalline anisotropy. However, this is based on bulk parameters. Imperfect stoichiometry in the YIG film would likely raise the magnetostriction as a result of the presence of magnetoelastic Fe ions with valence state other than 3+, which could provide a stronger out-of-plane contribution to the anisotropy.

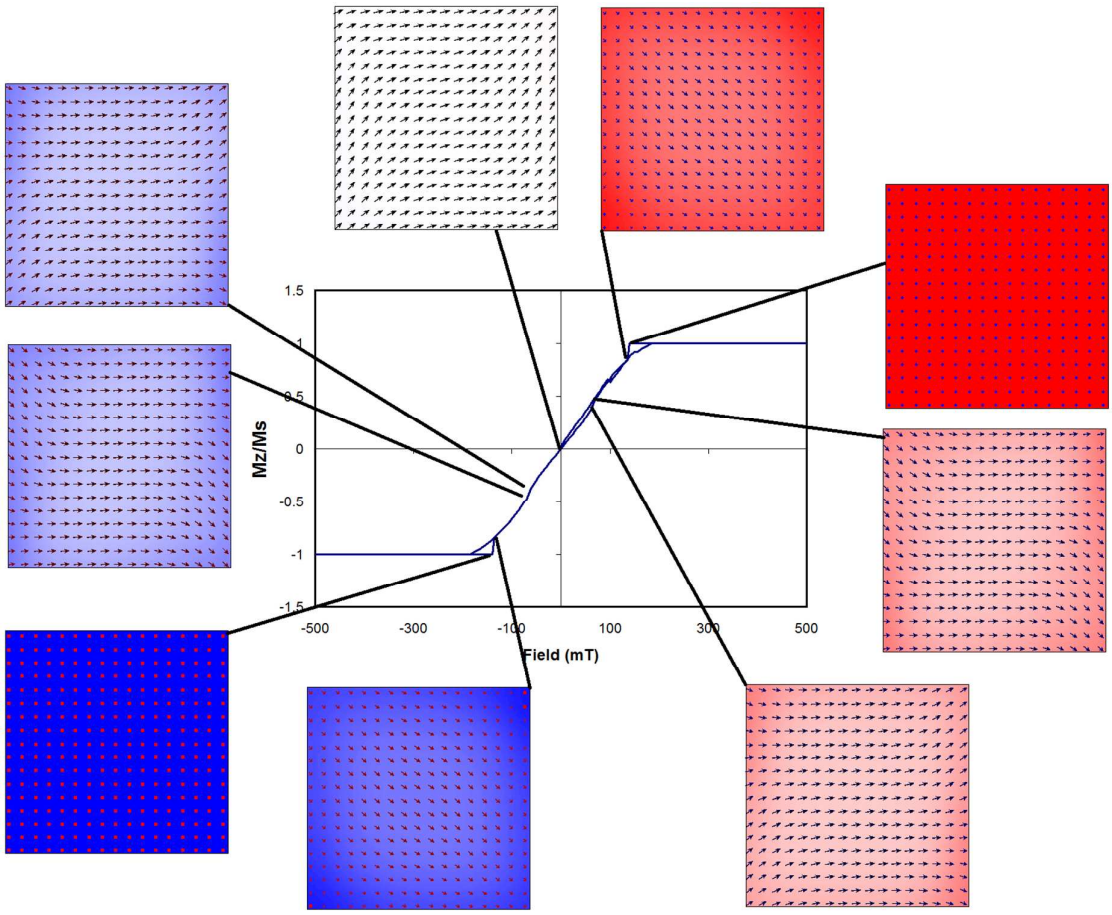

Figure S9. OOMMF model of YIG film, 1 μm square and 50 nm thick, for an out of plane field. Snapshots of the magnetic configuration are shown for different fields.

S10. MOKE measurements of GGG and Bi_2Se_3/GGG

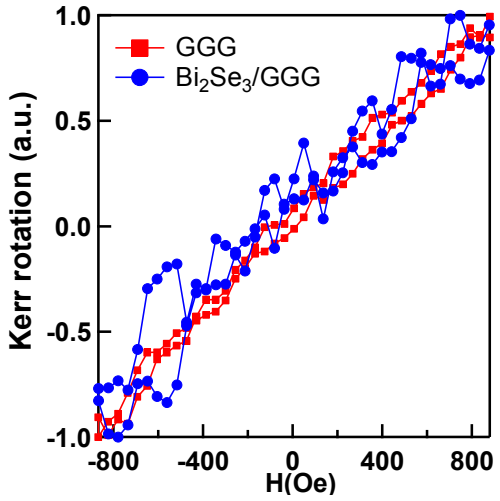

Figure S10. Longitudinal MOKE of GGG substrate and Bi_2Se_3/GGG showing a linear paramagnetic signal at T=77 K.

Reference:

1. Kong, D.; Cha, J. J.; Lai, K.; Peng, H.; Analytis, J. G.; Meister, S.; Chen, Y.; Zhang, H.-J.; Fisher, I. R.; Shen, Z.-X.; Cui, Y. *ACS Nano* **2011,** 5, (6), 4698-4703.
2. Lang, M.; He, L.; Xiu, F.; Yu, X.; Tang, J.; Wang, Y.; Kou, X.; Jiang, W.; Fedorov, A. V.; Wang, K. L. *ACS Nano* **2011,** 6, (1), 295-302.
3. Qu, D.-X.; Hor, Y. S.; Xiong, J.; Cava, R. J.; Ong, N. P. *Science* **2010,** 329, (5993), 821-824.
4. Eto, K.; Ren, Z.; Taskin, A. A.; Segawa, K.; Ando, Y. *Phys. Rev. B* **2010,** 81, (19), 195309.
5. Analytis, J. G.; Chu, J. H.; Chen, Y. L.; Corredor, F.; McDonald, R. D.; Shen, Z. X.; Fisher, I. R. *Phys. Rev. B* **2010,** 81, (20), 205407.
6. O'handley, R. C., *Modern magnetic materials: principles and applications*. Wiley New York: 2000; Vol. 830622677.
7. Geller, S.; Espinosa, G. P.; Crandall, P. B. *Journal of Applied Crystallography* **1969,** 2, (2), 86-88.
8. Sposito, A.; May-Smith, T. C.; Stenning, G. B. G.; de Groot, P. A. J.; Eason, R. W. *Opt. Mater. Express* **2013,** 3, (5), 624-632.
9. Clark, A. E.; Strakna, R. E. *Journal of Applied Physics* **1961,** 32, (6), 1172-1173.
10. Spencer, E. G.; Denton, R. T.; Bateman, T. B.; Snow, W. B.; Van Uitert, L. G. *Journal of Applied*

Physics **1963,** 34, (10), 3059-3060.